AIRBUS RACER – CFD ROTOR SIMULATION CHALLENGES AT HIGH SPEED

Enric Roca León, Airbus Helicopters, Marignane, France
Martin Embacher, Airbus Helicopters, Marignane, France
Damien Desvigne, Airbus Helicopters, Marignane, France
Paul Eglin, Airbus Helicopters, Marignane, France

Abstract

This paper presents a computational analysis of the Airbus Helicopters RACER main rotor at high speeds from 240kt up to 261kt, with a focus on predicting pitch link loads and inter-blade damper displacement. Numerical results are validated against flight test data. At these flight conditions, the stability of coupled CFD simulations is highly sensitive to the selected trim strategy, posing significant convergence challenges. Two trim strategies are investigated. The first is designed with high fidelity to the flight test procedure, wherein high speed was achieved through a shallow descent with a constant collective pitch, using airframe pitch as a trim variable. While accurately replicating the test condition, this approach induced limit-cycle oscillations in the simulation, which are attributed to phase variations of the computed shock on the advancing blade. A second, more conventional trim strategy employing only collective and cyclic controls demonstrated superior numerical stability, enabling simulation convergence. Although this method produced minor discrepancies in predicted control angles relative to the flight data, the resulting pitch link loads and damper displacements show good agreement with the measurements in flight up to 261kt.

1. NOTATION

Symbols

CP	Rotor shaft power coefficient
N_b	Number of blades
r	Radial position along the blade, m
R	Rotor radius, m
R_0	First airfoil span position, m
T	Main rotor thrust, N
V	Flight speed, m/s or kts
Z_S	Density altitude, ft
α	Aircraft incidence, deg
α_{TPP}	Tip path plane incidence, deg
β	Sideslip angle, deg
β_{1c}	Longitudinal flapping, deg
β_{1s}	Lateral flapping, deg
ϵ_i	Trim convergence error at iteration i
θ_0	Collective pitch angle, deg
θ_{1c}	Lateral cyclic pitch angle, deg
θ_{1s}	Longitudinal cyclic pitch angle, deg
ψ	Blade azimuth angle, deg
µ	Main rotor advance ratio
Ω	Main rotor speed of rotation, rad/s

Acronyms:

AH	Airbus Helicopters
BVI	Blade-Vortex Interaction
CFD	Computational Fluid Dynamics
CSD	Computational Structural Dynamics
DoF	Degrees of Freedom
ERF	European Rotorcraft Forum
H/C	Helicopter
ISA	International Standard Atmosphere
NR	Number of Rotations (main rotor)
RACER	Rapid and cost-effective rotorcraft
RANS	Reynolds-Averaged Navier-Stokes
URANS	Unsteady RANS

2. INTRODUCTION

The simulation toolchain employed in this study has been previously validated on the Airbus H175 helicopter rotor, as detailed in Ref. 4, showing excellent correlation with flight test data for conventional flight speeds. This paper extends the application of this validated toolchain to the significantly more demanding high-speed flight envelope of the RACER (Rapid and cost-effective rotorcraft). A key challenge for the compound formula is assessing whether an existing, conventional rotor can be used in this new, extended flight domain while maintaining an acceptable fatigue life for its components. The flight conditions are characterized by advance ratios $\mu = V/(\Omega R)$ approaching 0.6 and beyond, creating a complex aerodynamic environment with a large reverse flow region on the retreating blade, a phenomenon previously analyzed in detail for the X3 demonstrator (Ref. 14) and for slowed rotors at high advance ratios such as the UH-60 (Refs. 7,9,10,15). The primary objective of this work is therefore to simulate the RACER rotor at speeds of 240 knots and beyond to predictively analyze critical component loads, such as pitch link and inter-blade damper loads. A key focus of this investigation is to identify and address the numerical challenges, particularly concerning trim convergence and stability, that arise at these extreme flight conditions. Different trim strategies are explored, and their impact on simulation stability and the physical realism of the results is discussed.

The RACER demonstrator performed its first flight in April of 2024, a flight that did not reveal major technical obstacles and confirmed good handling in wind up to 20kts. Progress towards high speed thus was made quickly, and the classical h/c speed domain was left behind already at the third flight, reaching 170kt of TAS. The projected cruise speed of VH = 220kt TAS could be validated during flight seven, where 225kt of TAS were demonstrated. Prior to this flight, the main-rotor full fairing had not been installed. The drag reduction it provides offers a greater margin for achieving higher speeds.

Based on the X3 program experience and taking into account the projected operational cruise speed a verification of a design-dive speed of 261k was deemed necessary. The corresponding flight test was carefully prepared, relying deliberately on the simulations presented in this paper in order to check trends in rotor and blade loads beforehand. A test point stabilized at 261kts during 10s was flown during flight 15, and in connection with the RACER NR-law results in an advance ratio of $\mu = 0.689$ and an advancing-blade tip Mach-number of Ma = 0.982.

The main rotor full fairing (see Figure 1) had been installed during this flight. In order to contextualize these rotor parameters, the maximum advance ratios and advancing-blade Ma-numbers of previous rotorcrafts with lift- and thrust- compounding are listed below.

Figure 1: RACER demonstrator aircraft

Table 1: Rotor tip Mach number and advance ratios for comparable compound formulas.

Aircraft	V [kt]	μ	Ma
Lockheed XH-51A (Ref. [17])	263	0.716	0.942
Bell HPH (Ref. [18])	275	0.718	0.994
Lockheed AH-56A (Ref. [18])	242	0.65	0.928
Airbus X3	263	0.67	1.02
Airbus RACER	261	0.70	0.982

3. NUMERICAL METHODOLOGY

The simulation approach is based on a loose coupling between the DLR FLOWer CFD solver (Ref. 4, 5,8) for aerodynamic load prediction and the CAMRAD II comprehensive analysis code (Ref. 2) for rotor trim and structural dynamics. The overall simulation strategy is depicted in Figure 2.

3.1. CSD Solver: CAMRAD II

CAMRAD II is a comprehensive rotorcraft analysis code that incorporates multibody dynamics, nonlinear finite element modeling for structural dynamics, and low-fidelity aerodynamics. In this toolchain, CAMRAD II is responsible for calculating the main rotor structural response, including blade elastic deformations, and determining the control inputs (collective and cyclic pitch) required to trim the helicopter to a specified flight condition.

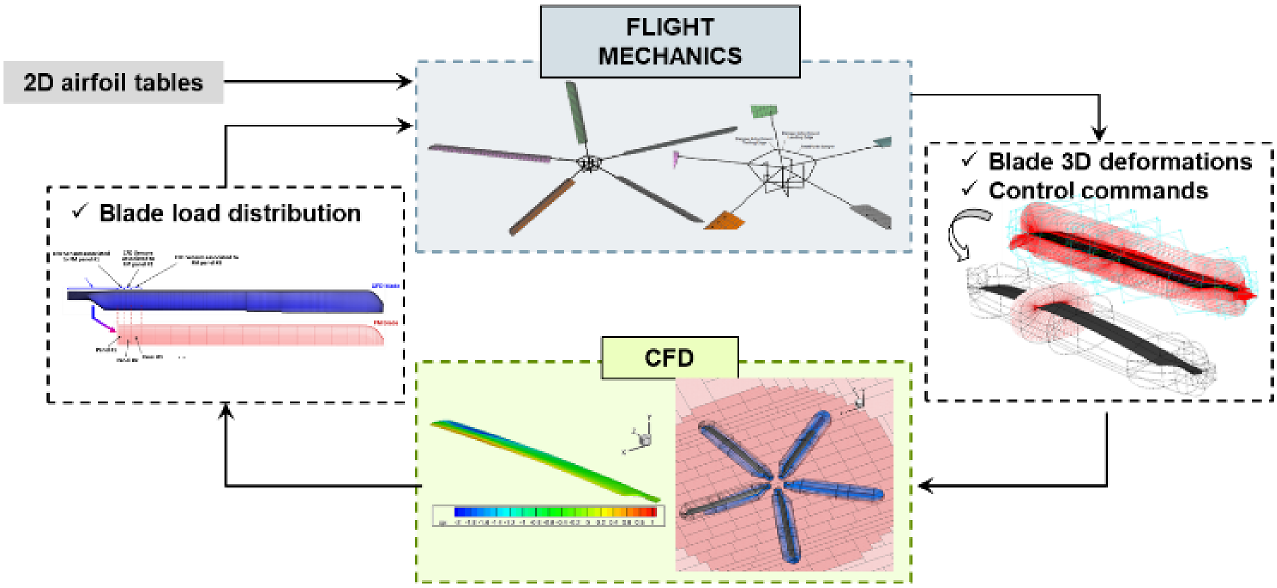

Figure 2: Overview of the simulation strategy

The CSD model for the RACER rotor is based on previous work on the H175 (presented in detail in Ref. 3), and includes a full elastic representation of the main rotor blades and a detailed model of the inter-blade dampers.

In the current work, the structure dynamics solution is sought using a Newton-Raphson algorithm considering 10 blade modes with 10 harmonics for all CAMRAD II output quantities, taking into account 30 rotor azimuthal positions per revolution (12° azimuthal timestep).

3.2. CFD Solver: FLOWer

The aerodynamic blade loads are computed using the FLOWer code (Ref. 13), which solves the Unsteady Reynolds-Averaged Navier-Stokes (URANS) equations on a block-structured grid. The turbulence is modeled using Menter's Shear Stress Transport (SST) k-ω model (Ref. 6). The time-dependent solution is advanced using an implicit dual time-stepping method. The ROT extension in FLOWer manages the blade motion and deformation, which are prescribed by the CSD solver at each time step.

3.3. CFD Model and grid

The CFD analysis is performed on an isolated rotor model. The blade geometry, including the specific tab arrangement shown in Figure 3 is accurately represented. A multi-block structured grid with approximately 5.9 million nodes is used for each blade. The complete computational domain utilizes a Chimera overset grid approach to embed the blade grids within a background mesh, allowing for the simulation of blade rotation and elastic deformations.

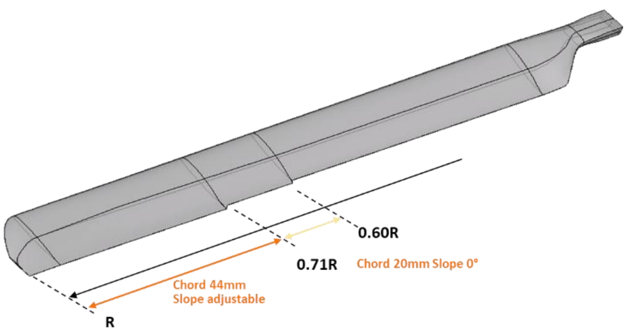

Figure 3: RACER Tab implementation. the slope angle of the tab (in the span range from 0.71R to R) is adjustable.

3.4. CSD/CFD Coupling and Trim Procedure

A loose-coupling procedure is employed, where aerodynamic loads from FLOWer are iteratively fed back to CAMRAD II. CAMRAD II uses these high-fidelity loads to update the helicopter trim and blade structural deformations, which are then passed back to FLOWer for the next aerodynamic calculation. This cycle continues until a converged solution for both the aerodynamic loads and the helicopter trim is achieved.

This work utilizes a 3-DoF trim for an isolated rotor, where trim targets (e.g., thrust, propulsive force) are specified. This contrasts with a full-helicopter 6-DoF trim (as used in Ref. 12), where the trim task is to cancel the total forces and moments on the complete aircraft by varying main and tail rotor controls as well as aircraft attitude. A significant challenge at very high speeds (240 kt and above) is achieving a stable, converged trim solution. The choice of trim strategy has a significant impact on convergence. In this work, two primary strategies were investigated:

- **Airplane Trim Law**

  This strategy uses a converged 210kt level flight simulation as a starting point. The collective pitch is fixed at the converged value, and the simulation is trimmed for a higher speed by varying the airframe /rotor inclination and cyclic commands to meet targets for blade flapping and thrust. This trim law is coherent with dive maneuvers, as the pilot will generally keep a constant collective stick during acceleration to cruise velocity and in a subsequent dive maneuver, and it can be assimilated to an airplane trim. This approach is well suited for reusing flight test data (which typically include collective, cyclic controls and H/C attitudes) and matching it with a simulation a-posteriori. However, at high speed and advance ratios this approach proved difficult to converge, often resulting in undamped oscillations in the trim variables.

- **Helicopter Trim Law**

  This is a more conventional approach where the trim degrees of freedom are the collective and cyclic pitch angles, with targets in our case set for zero flapping and a thrust level that accounts for wing/rotor lift compounding. This strategy was considered to be best suited to predict general loads before flight, as nearly zero flapping and aircraft incidence are the nominal conditions foreseen for the RACER aircraft, and provided a simple framework for comparing the rotor behavior at increasing speeds. Additionally, this strategy was found to be significantly more stable.

Numerical techniques such as applying relaxation between trim iterations and refining the azimuth discretization in the CAMRAD II model were also explored to damp the numerical oscillations when present.

4. RESULTS AND DISCUSSION

The analysis begins with a discussion of the instabilities encountered with the first (occasionally unstable) trim approach, followed by results from the stable trim strategy and by flight test comparisons.

4.1. Flight cases

Using an existing computation at 210kt, which had been presented in Ref.1, a progressive increment in speed was simulated to predict the load gradients towards higher speeds

For this purpose, computations at 240, 255 and 261kt were performed using different trims and covering a range of advance ratios of μ=0.55 – 0.70.

The computations were run at standard atmosphere and 6000ft with adjusted wing/rotor contributions for each case targeting main rotor thrust objectives while maintaining zero flapping.

Table 2: Considered trim strategies and flight cases.

	Trim DoFs	**Trim targets**	**TAS [kt]**
Airplane Trim Law	PITCH LNGCYC LATCYC (fixed COLL)	T_{MR} $\beta_{1c}=0$ $\beta_{1s}=0$	240
			255
Helicopter Trim Law 6000ft ISA	COLL LNGCYC LATCYC	T_{MR} $\beta_{1c}=0$ $\beta_{1s}=0$	210
			240
			255
			261

As thrust objective for 210kt, the nominal design value for this speed was selected. The thrust objectives for the higher speeds have been obtained by computations with the comprehensive code STORM, an AH inhouse code based on the code HOST (Ref. 11). Main rotor collective, propeller power and stabilizer setting were maintained at the 210kt value, while speed was increased in exchange for descent rate. The simulated aircraft pitch equilibrium variation with speed determines the wing lift through small changes in aircraft incidence and longitudinal flapping in the order of $\Delta\alpha$ = 0.1deg and $\Delta\beta_{1c}$ = -0.4deg, and thus leads to a diminishing main rotor thrust, reduced by 17% at 255kts. Nevertheless, β_{1c} = 0 was prescribed for simplicity, because initially it was expected to apply the aircraft trim law with its trim on pitch attitude / incidence.

4.2. Trim Instability at High Speed

When employing the first trim strategy (used for simulating a dive entry), the solution failed to converge and entered a limit-cycle oscillation or divergent states for 240+kt simulations.

Figure 4 shows the trim variables evolution with the coupling iterations for cases at 240kt and 255kt. The pitch values are shown to diverge or oscillate (with an amplitude of up to 1.5°) combined with lateral cyclic variations.

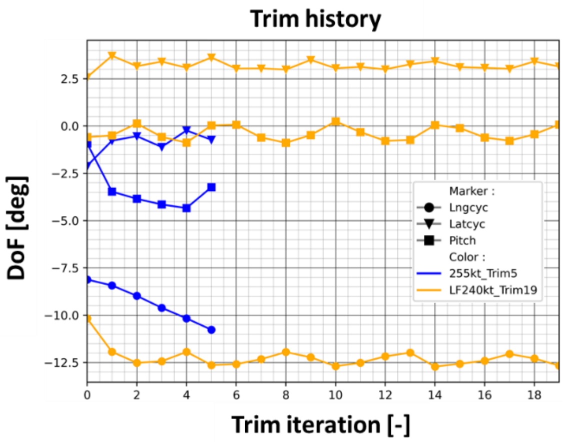

Figure 4: Trim variables evolution with coupling iterations for 240kt (orange) and 255kt (blue).

Figure 5 shows the variation of the pitch-link loads over four successive trim iterations at 255kt. The loads do not settle on a single solution, instead hopping between different states.

This numerical instability is directly linked to the elastic torsional behavior of the blade. Figure 6 shows the elastic pitch deformation of the blade for the last two trim iterations and the sectional torsion moment. A distinct jump in the phase of the torsional deformation (approximately 12°-15°) is observed between iterations with increasing amplitudes. This rapid change in the blade's aeroelastic response prevents the trim algorithm from finding a stable equilibrium, leading to the oscillating loads seen in Figure 5.

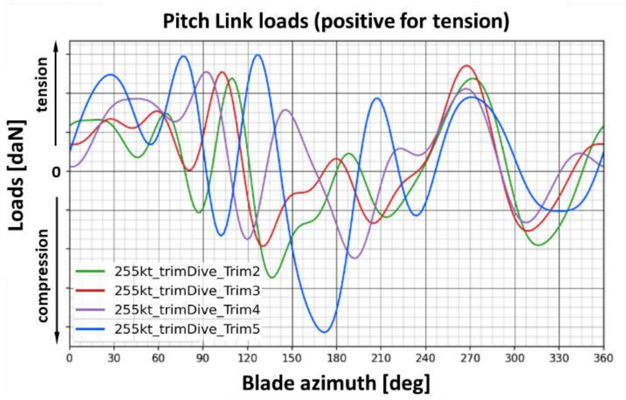

Figure 5: Pitch link loads evolution showing trim instability at 255kt

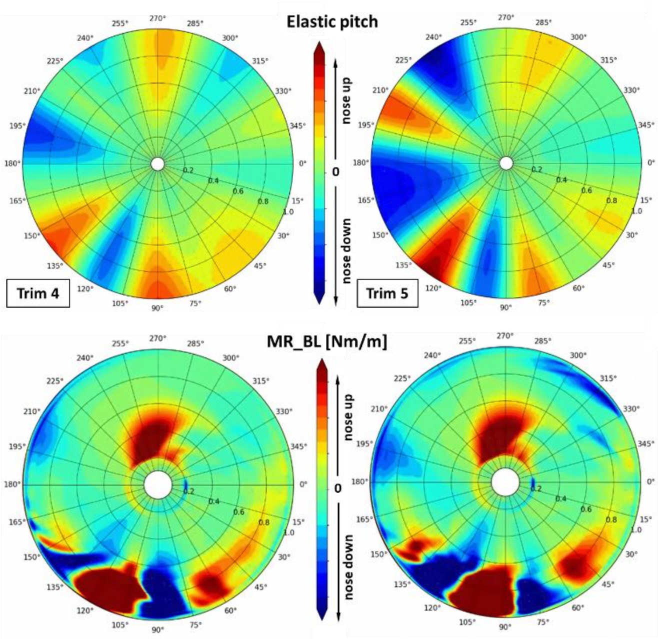

Figure 6: Elastic torsion in the blade pitch axis (top) and sectional pitch moment (bottom) as a function of radius and blade azimuth ψ at 255kt for the last two trimmed iterations

This numerical instability phenomenon can be traced back to the highly sensitive transonic flow physics on the advancing blade. At such high forward speeds and tip Mach numbers (0.954 - 0.977 for 240kt - 255kt respectively), a shock wave develops on the outboard portion of the blade both on the upper and lower surfaces of the airfoil. The precise location and strength of these shocks are critical to the overall aerodynamic loads but are difficult to compute, as they depend on a multitude of parameters including the local angle of attack and blade elastic deformation. Precisely this local angle of attack in the advancing blade is a function of longitudinal cyclic and pitch, which occasionally vary by more than 2° between trim iterations. A visualization of the shock at two radial stations is presented in Figure 7 for the last two iterations of the 255kt case.

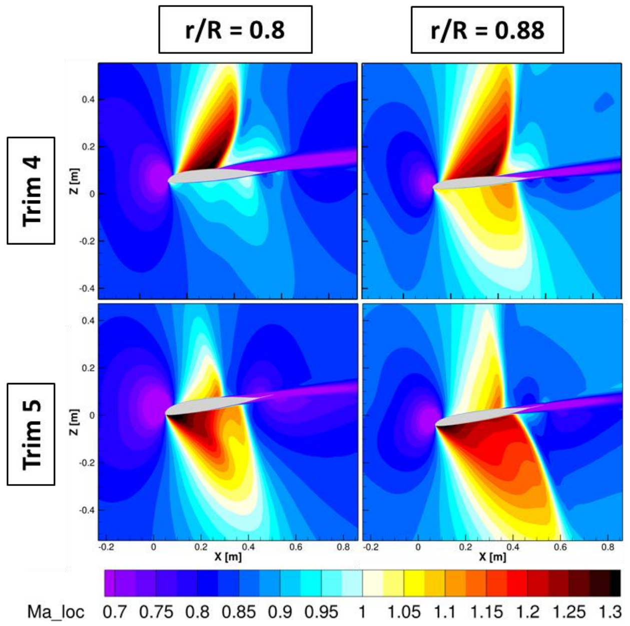

Figure 7: Local Mach number contours at blade azimuth ψ =90° for the last two converged trims at 255kt and radial sections 0.8R (left) and 0.88R(right).

It is observed that between iterations, a change in blade pitch on the advancing side causes the preponderant shockwave to jump from the upper surface (extrados) to the lower surface (intrados). This reverses the blade's sectional pitch moment and the airfoil center of pressure in that azimuthal sector, forcing CAMRAD II into a correction loop. It is supposed that the pitch moment variations of the CAMRAD II aerodynamics model are substantially differing from the CFD model, such that the blade torsion and trim suggested by CAMRAD II for the next trim iteration do not yield a progress towards the dynamic equilibrium state under CFD loads. Such mismatches in gradients theoretically are a source of instability of a coupling scheme if they are exceeding a certain threshold, usually a mismatch by a factor greater than 2 or less than 0.5. However, these thresholds are only indicative in our case, since the degrees of freedom of the coupling (rotor trim and blade motion) are not independent, and sufficient stability on one degree of freedom can compensate instability on another. In the present case, the trim seems to be extremely sensitive to the elastic torsion DoF and to pitch angle variations.

This unstable behavior translates into a divergence of the delta loads between CFD/CSD codes as shown in

Figure 8, where a metric for rotor thrust error between codes is used. The trim convergence error metric at iteration i, denoted as ϵ_i, is defined as the maximum value over a complete rotor revolution of the combined spatial L2 norm of the sectional error thrust summed across all blades.

In details, the sectional error thrust $\Delta T'_{i,b}$ for each blade b is the difference between the loads predicted by CFD $T'_{CFD,i,b}$ and the corrected thrust from the lifting-line model on the CSD side $T'_{CSD\mathrm{corr},i,b}$:

$$\Delta T'_{i,b}(r,\psi) = T'_{CFD,i,b}(r,\psi) - T'_{CSD\mathrm{corr},i,b}(r,\psi)$$

The total error metric ϵ_i is then calculated by taking the maximum over all azimuth of the root sum of squares of the individual blade thrust norms:

$$\epsilon_i = \max_{0\le\psi\le2\pi}\left(\sqrt{\sum_{b=1}^{N_b}\int_{R_0}^{R}\left(\Delta T'_{i,b}(r,\psi)\right)^2 dr}\right)$$

Similar behavior is obtained at 240kt, albeit with the difference that limit cycle oscillations are reached instead of divergence.

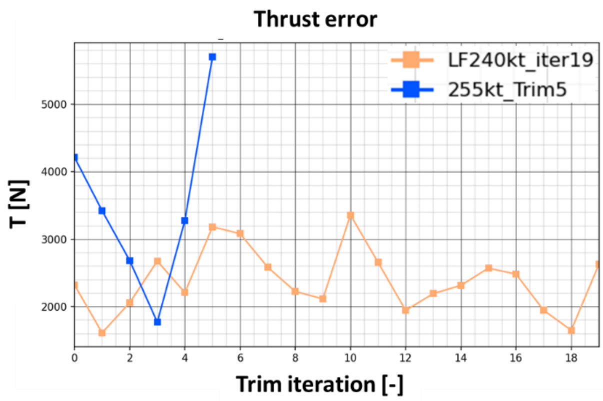

Figure 8: Error correction metric on rotor thrust between trim iterations for the unstable trim at 255kt (blue) and for the 240kt case (orange).

The sectional thrust of this unstable solution is presented in

Figure 9. The lift producing zones are phased by ~12-15° between iterations coherent with the elastic

torsion variations. It is not clear whether the origin of the oscillation can be found in the structural modelling or on the CFD computation. Capturing the transonic shock is challenging on CFD specially using industrial settings (i.e. RANS with relatively large time stepping).

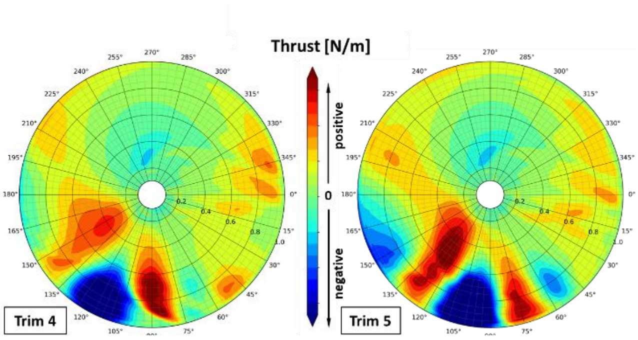

Figure 9: Sectional thrust as a function of radius and blade azimuth ψ at 255kt for the last two iterations.

The modal basis used on the CSD to trim the computations combined with the limited harmonics might filter out local effects. In order to investigate this, additional studies are on-going, refining the CAMRAD II azimuthal discretization from 12° to 3° and increasing the harmonics from 10 to 20 as well as reducing time stepping on CFD side. However, using this numerical setup the simulation time of the CSD computations increase significantly and thus reach the same order of wall-clock time as CFD computations due to the difficulty in converging the inter-blade damper configuration. These results are out of the scope of this work.

Stabilized simulations were achieved using the second trim strategy, which provided reliable results that could be employed in further analysis and comparison with flight data. Furthermore, using these stabilized converged computations as a starting point, a subsequent trim with the helicopter pitch also provided stable results if no vertical speed was included.

4.3. Helicopter cruise stable trim

The error metric presented beforehand shows a good convergence of the errors between coupling iterations for all the considered speeds using the second trim strategy, as presented in Figure 10. Imposing a flat rotor disk with respect to the incoming flow eliminates the oscillations caused by the transonic shocks, since the computations seem much less sensitive to collective angle rather than pitch. For comparison with the unstable simulations, the converged result in terms of local Mach is provided in Figure 11 at the blade tip for the 255kt case.

The maximum local Ma number remains below 1.25, and the shock foots are located near the trailing edge with much less dissymmetry between the upper and lower airfoil surfaces.

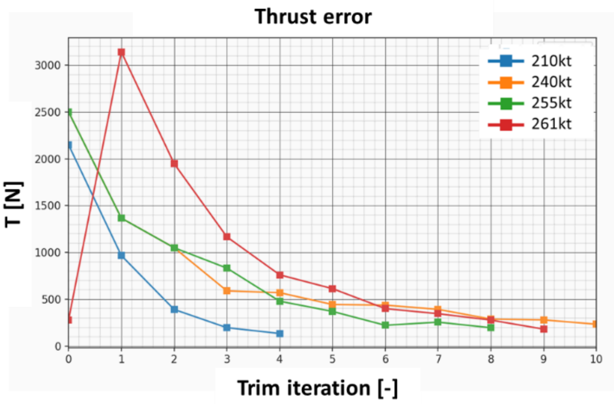

Figure 10: Error correction metric on rotor thrust for 210-261kt simulations.

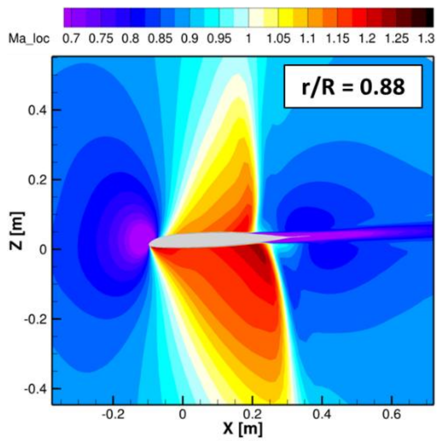

Figure 11: Local Mach number at the advancing blade (ψ=90° r/R=0.88) at 255kt for the stable trim strategy

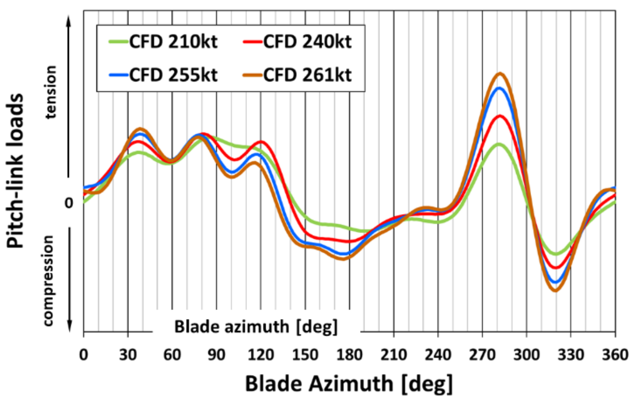

Figure 12 compares the resulting main rotor pitch-link loads against the baseline 210kt case. The results show a clear evolution in the load profile with the increase in speed, with the reversed flow region increasing the nose up moment at the retreating blade followed by a nose down moment due to the local stall and elastic rebound.

The harmonic breakdown shows a steady increase in the amplitudes over the entire spectrum (see Figure 13) at virtually the same phases (not shown).

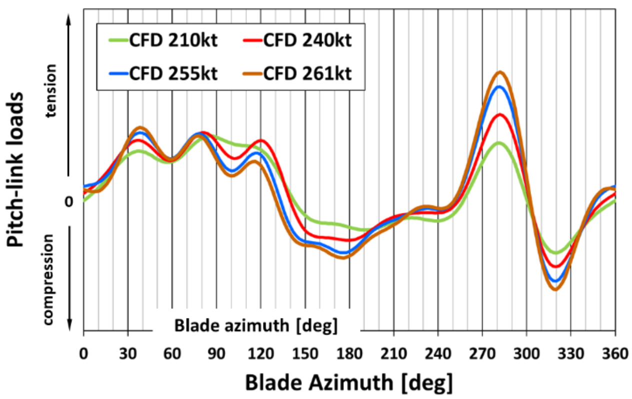

Figure 12: Pitch link loads evolution with speed as a function of the blade azimuth ψ, obtained with the helicopter trim law.

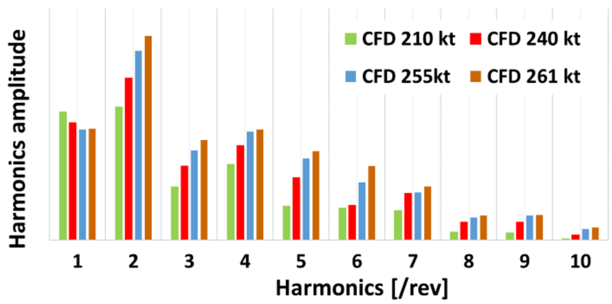

Figure 13: Pitch link loads harmonic breakdown as a function of speed.

The loads are dictated by two distinct phenomena on opposite sides of the rotor disk detailed in the following paragraphs.

Advancing Side Transonic Effects

On the advancing side (Ψ≈90°), the blade tip operates in a transonic regime. The negative lift peak is increased with speed as expected, see Figure 14. Transonic effects can be observed indirectly in form of the sectional pitch moments, which are shown in Figure 15. From 240kt onwards, a nose-up moment appears at blade sections outboard of 0.8R at the advancing blade. These transonic effects in the advancing blade are observed for 240+kt simulations. A visualization of local pressure at the blade tip is presented in Figure 16. The center of pressure of the airfoil is displaced rearwards as an effect of the intrados shock producing, in combination with negative lift, a strong local nose up moment. This is combined with an interaction with a vortex created in the second quadrant, whose trace is clearly visible in the pitch moment contour diagram for the 210kts case around Ψ = 90°…100° (Figure 15); on one hand, this vortex intensifies negative lift on its outboard side, as it is shed at the negatively loaded preceding blade tip (for details on the mechanism, see for instance the discussion in Refs. 15 and 14); on the other hand, it appears to generate a nose-up moment at least in the 210kts case, as shown in Figure 15. On the other hand, transonic shocks at more inboard regions (r/R = 0.65…0.8, see Figure 17) of the advancing blade produce, in combination with positive lift, locally strong nose down moments counterbalancing those of the tip region.

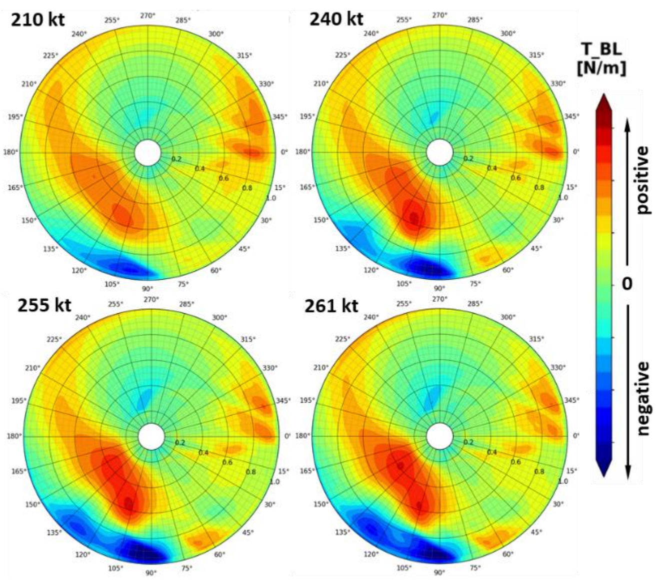

Figure 14: Sectional thrust for 210-261kt.

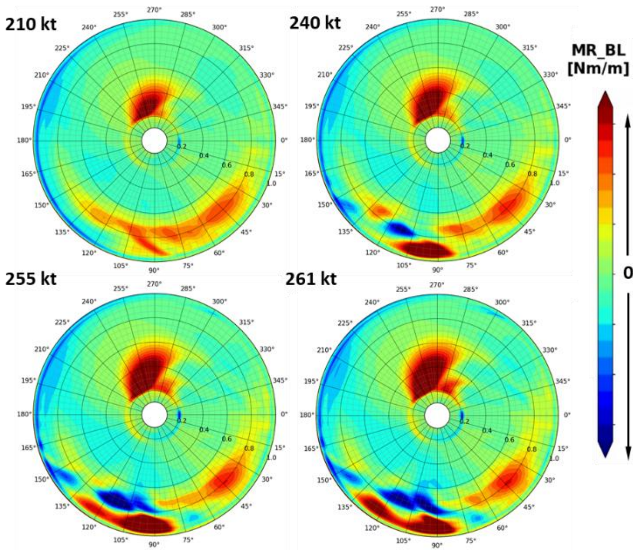

Figure 15: Sectional pitch moment for 210-261kt (positive for blade nose-up).

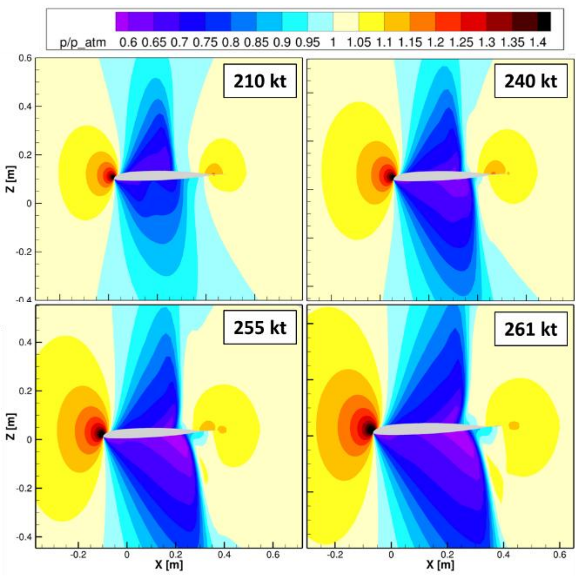

Figure 16: Pressure contours at 0.88R and Ψ=90° for pitch for 210, 240, 255 and 261kt.

The blade tip experiences an intensifying nose-down pitching moment starting around Ψ≈105° (interrupted shortly at Ψ = 120° for the 240+kt cases), which might be related to the gradual compression of the pitch link from Ψ ≈ 120° until Ψ ≈ 150°, provided that inertial effects introduce no significant delay, and there are no other antagonistic mechanisms.

The aerodynamic moment gradient is highlighted well by the temporal derivative of the sectional pitch moment presented in Figure 18. Using this metric, the BVI in the advancing blade region is clearly identified at 210kt around Ψ = 90° and the rear blade position. Also, for the 255kt and 261kt cases, traces of BVI at these two locations appear.

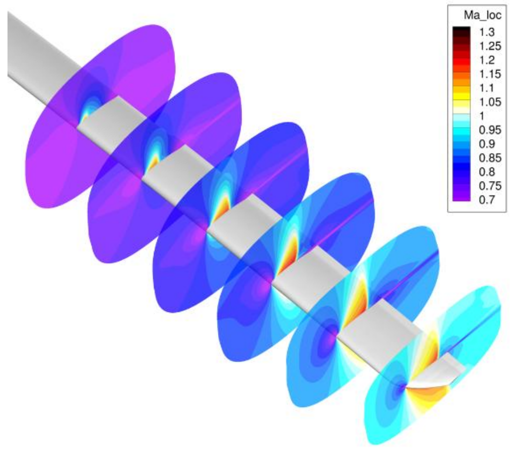

Figure 17: Local Mach number at the advancing blade (ψ=90°) at 255kt for the stable trim strategy.

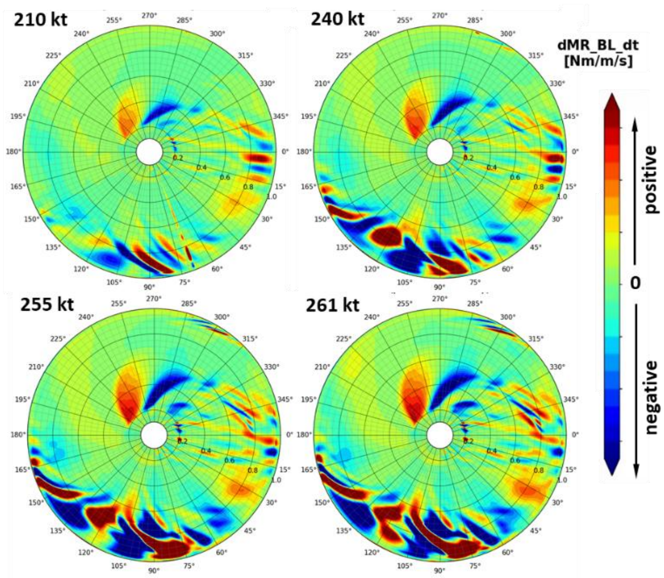

Figure 18: Sectional pitch moment time derivative for 210-261kt (positive for blade nose up gradient).

Retreating Side Reverse Flow and Stall

On the retreating side (Ψ≈270°), the blade experiences a large region of reverse flow covering up to μ_{max} = 70% of the blade radius. Figure 15 shows the dominating effect on sectional pitch moment of the reverse flow region.

The retreating blade experiences stall in connection with a vortex shed from the trailing edge and propagating below the blade, amplifying the nose-up pitching moment. Following the vortex shedding, an elastic rebound produces a strong inertial nose-down moment. A detailed analysis of the reverse flow region and the trailing edge vortex physics was discussed in detail in Refs. 14-15 and presented as well in Ref 1 at 210kt and is thus not reproduced here. The phenomena remain the same at higher speeds with increasing intensity. As a result, the peak-to-peak value of the pitch link loads increases steadily with the speed and is driven by the retreating blade nose-up peak and the nose-down elastic rebound.

Increased BVI can be observed near the rear blade position for higher speeds, as visualized in Figure 20 and Figure 20 with no significant effect on the pitch link loads.

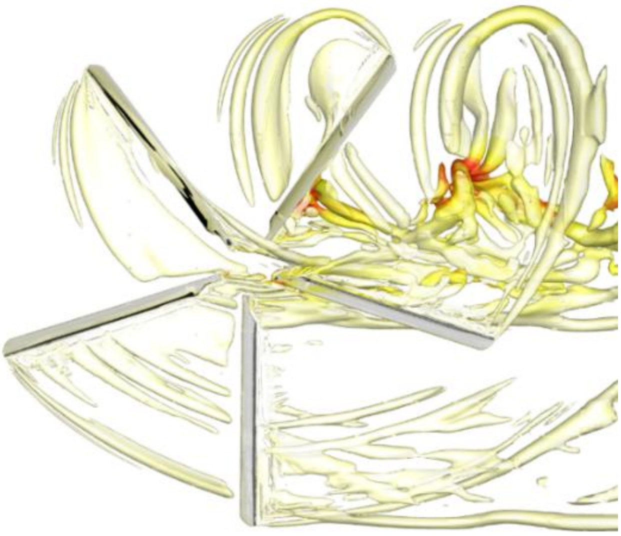

Figure 19: Q-criterion iso-surface colored by the turbulent viscosity ratio μ/μ_t for 210kt.

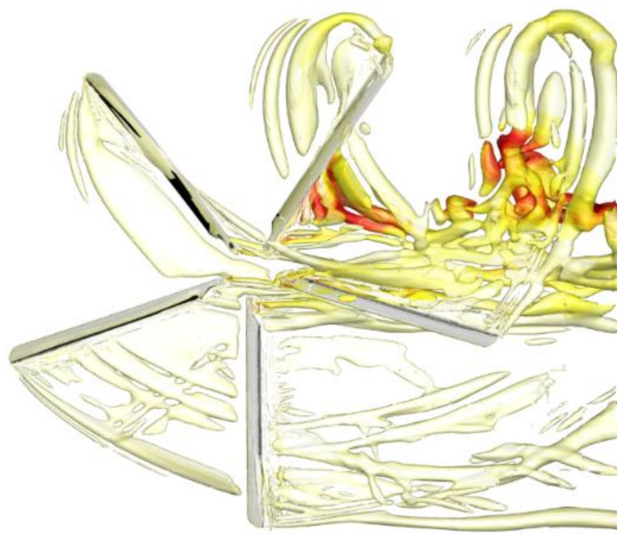

Figure 20: Q-criterion iso-surface colored by the turbulent viscosity ratio μ/μ_t for 261kt

4.4. Flight test comparisons

The flight test point with 261kt was recorded while the RACER was in descent. The test point was stabilized during 10s, and the density altitude was Z_S = 3600ft in average. This differs from the simulation, where Z_S = 6000ft had been chosen as the uniform condition for all simulation cases. Normalized rotor lift deviates by $\Delta Ct/\sigma = Ct/\sigma_{CFD} - Ct/\sigma_{FT} = 0.003$. Note that rotor lift is measured on the RACER, as described in detail in Ref. 1. Tip Mach numbers of the advancing blade are similar, Ma = 0.987 in the simulation vs. Ma = 0.982 in flight. Given the impact of transonic effects on blade pitch motion adressed in the previous pragraph, this similarity is beneficial for an assesment of the prediction of pitch link loads.

Rotor control and flapping angles of the 261kts case are compared in Table 3. Blade flap angles β are defined positive for downward flapping.

Table 3: Control angles of flight test and simulation in comparison, 261kts.

261kts	θ_0	θ_{1C}	θ_{1S}	β_{1c}	β_{1S}	α
Flight Test	2.5°	4.5°	-9.3°	1.2°	-4.6°	0.1°
Simulation	2.1	-1.0°	-10.5°	0°	0°	0°

An offset can be noted particularly for the lateral flapping (β_{1s}), which is characterized by a considerable inclination of the rotor plane to the right in case of the flight test. This explains why a pronounced right lateral cyclic (θ_{1c}) is present in flight. The need for a roll-right moment in flight probably has two explanations: First, rotor-wing interaction is asymmetric, leading to higher lift on the right wing (see for instance ref. 16). Secondly, the flight was conducted with a sideslip of β = 2° nose-left, which further raises right wing lift because of a dihedral effect.

This sideslip had not been anticipated when setting up the trim law for the simulations. It is itself partially a consequence of the wing roll moment, since the lateral rotor force from disk tilt (β_{1S}) needs to be equilibrated by lateral force to the left on the airframe. Furthermore, the wing lift difference generates, due to the asymmetry in static pressure above the wings, a rightwards side force on the fuselage, which needs to be compensated by nose-left sideslip as well. A third contributor is suspected in the form of an asymmetry in total pressure below the rotor disk, that arises due to the low lift in the reverse flow circle and exerts a lateral force on the airframe, notably the rotor pylon.

Aircraft incidence in flight remained very close to zero at 261kts. The rotor disk angle-of-attack can thus be directly inferred from β_{1c}, and is slightly positive (α_{TPP} = 1.3°), while disk incidence is exactly zero in the simulation. This explains in parts the stronger forward cyclic input in the simulation; the resulting smaller control plane incidence, however, would require a higher collective, in particular since the non-dimensional thrust target is slightly above the flight value ($\Delta Ct/\sigma$ = 0.003). This offset cannot be explained currently, and might have its origin in elastic blade torsion, rigging/measurement procedures, modeling of the control kinematics, and infinite control stiffness in the model.

A shaft power difference of $\Delta CP = 7.0*10^{-5}$, on the other hand, is in line with the difference in α_{TPP}, as more propulsive power is to be spent in the simulation. Assuming that the thrust vector indeed tilts by α_{TPP}, a power difference of $\Delta CP = 6.4*10^{-5}$ is estimated when using the simple propulsive power calculation $\Delta P = \sin(\alpha_{TPP}) * T * V$.

Referred to the tip path plane, and neglecting any elastic torsion, the advancing blade (at Ψ = 90°) assumes a pitch angle of $\Theta_0 + \theta_{1S} - \beta_{1C}$= -8.0° in the flight test, and -8.4° in the simulation. For the retreating blade position Ψ = 270°, these rigid blade pitch angles are $\Theta_0 - \theta_{1S} + \beta_{1C}$= 13.0° in the flight test, and 12.6° in the simulation. Hence, apart from the (unknown) deviations in blade elastic torsion, the operating conditions of the blade tip at both the lowest and highest (transonic) relative airspeed appear to be well replicated by the simulation.

For the 240kt case, Table *4* summarizes the comparison in terms of control and blade flapping angles.

Table 4: Control angles of flight test and simulation in comparison, 240kts.

240kts	θ_0	θ_{1C}	θ_{1S}	β_{1c}	β_{1S}	α
Flight Test	2.8°	4.5°	-9.7°	1.1°	-2.8°	1.2°
Simulation	1.3°	-0.5°	-9.8°	0°	0°	0°

In contrast to the atmospheric conditions of 6000ft ISA foreseen in the simulation, this test point was conducted at a density altitude of approximately Z_S = 11000ft. Since the wing flaps were not in use, this means that also the rotor lift differs significantly, by $\Delta Ct/\sigma = Ct/\sigma_{CFD} - Ct/\sigma_{FT}$ = -0.025. Advancing blade tip Mach number and advance ratio are identical, however.

As already discussed for the 261kts, the flight test is characterized by a rightward inclination of the rotor plane. A deviation in θ_{1C} hence is not surprising, although this offset is slightly more pronounced in the 240kts case when referred to the theoretical TPP: $\theta_{1C,TPP} = \theta_{1C} + \beta_{1S}$ = 1.7° for the flight test, and -0.5° in the simulation (note the sign convention for β: Downward is taken positive). This might be a result of the higher non-dimensional rotor thrust of the flight test, leading to a stronger inflow in the rear half of the rotor disk. Absolute values of thrust are similar, hence the coning angles are expected to differ only by little and thus would not contribute a differing need for lateral cyclic.

Longitudinal cyclic trim is identical, whereby the real aircraft had assumed a positive angle of attack, and it also featured more rearward inclination of the rotor disk. A (rigid blade-) rotor disk incidence of α_{TPP} = 2.3° results, which means a significant difference compared to the zero angle of attack of the rotor plane in the simulation. A rise in collective is, however, still necessary to produce the relatively high thrust coefficient.

The advancing blade (at Ψ = 90°) assumes a rigid-blade pitch angle of $\Theta_0 + \theta_{1S} - \beta_{1C}$= -8.0° with respect to the theoretical tip path plane in the flight test (same value as at 261kts), while -8.5° are obtained in the simulation. Given that, additionally, the airframe is at positive angle-of-attack, less negative lift and lower-side compressibility effects at the tip can be expected for the flight test, provided the negative lift predicted by the simulation (see Figure 16 and Figure 14) is correct.

At Ψ = 270°, the pitch angles referred to the tip path plane are $\Theta_0 - \theta_{1S} + \beta_{1C}$= 13.6° in the flight test, and 11.1° in the simulation.

The pitch-link loads for the simulated cases and their comparison with flight test data are provided in

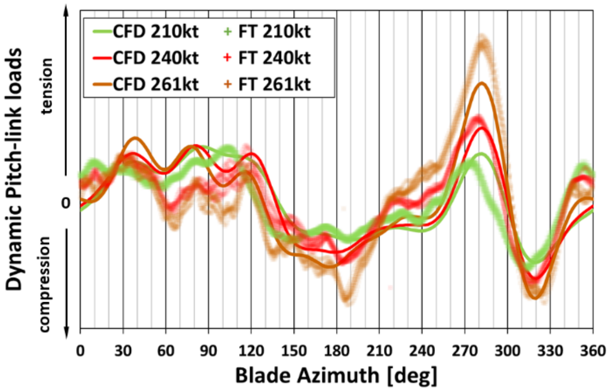

Figure 21 and their corresponding harmonic breakdown in Figure 22.

The simulation demonstrates a good correlation with the measured pitch link loads, capturing the primary physical drivers of the peak-to-peak amplitudes. Minor discrepancies can be attributed to the variations in flight conditions between the simulation and test data, particularly the density altitude for the 240kt case.

A harmonic analysis reveals that the amplitudes of the 1/rev, 2/rev, and 3/rev components do not diverge with increasing airspeed. A notable observation is the more intense negative load peak near the front blade (Ψ=180°) preceded by higher harmonic content in the flight data, which cannot be fully explained by purely aerodynamic pitching moments.

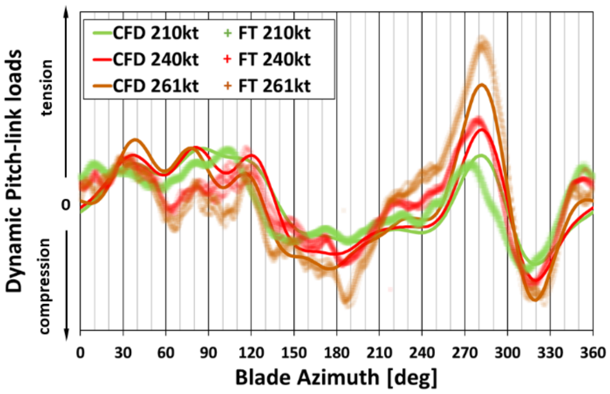

Figure 21: Comparison between CFD and FT data: pitch link loads as a function of the blade azimuth for 210, 240 and 261kt.

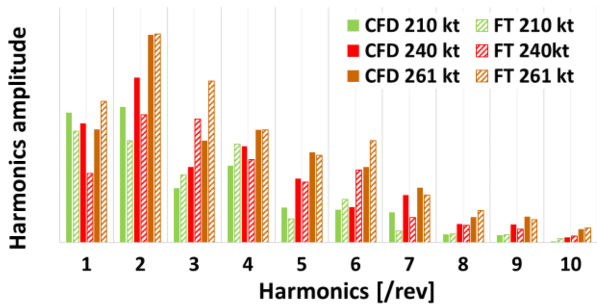

Figure 22: CFD vs FT data: Pitch link loads harmonic breakdown as a function of speed.

This suggests the influence of the flap-lag-torsion coupling mentioned above, where the significant downward bending of the blade tip under high drag and induces a torsional moment around the pitch hinge. Downward bending moments recorded at 0.65R, discussed below, reach their maximum at this location (cf. Figure 26 and Figure *28*).

Concerning damper displacement, a similar analysis as for the pitch link loads is performed in Figure 23 and Figure 24. The 1/rev, 2/rev, and 3/rev components increase with speed but remain well-behaved and are slightly overpredicted by the simulation. Peak-to-peak values are correctly predicted.

This completes the trends previously established in Ref. 1 in comparison with a conventional helicopter, now also showing the damper displacement harmonics up to 261kt (see Figure 25).

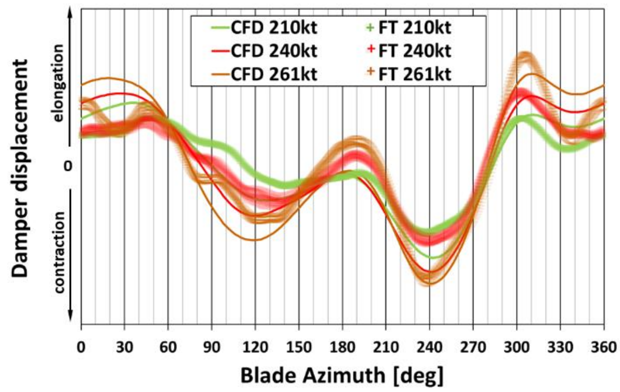

Figure 23: Comparison between CFD and FT data: dynamic damper displacement as a function of the blade azimuth for 210, 240 and 261kt.

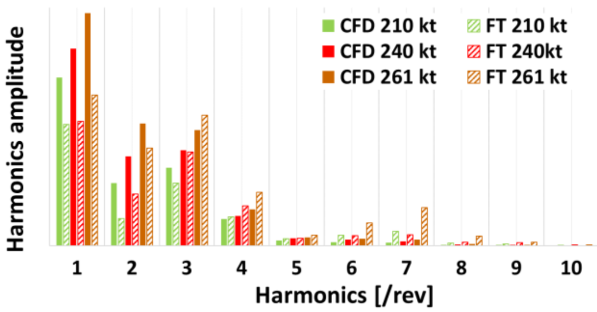

Figure 24: CFD vs FT data: Damper displacement harmonic breakdown as a function of speed

The effect of the compound formula clearly appears on the 1/rev component: offloading propulsion and lift from the main rotor prevents the typical increase of this component, keeping its amplitude relatively constant up to 240 kts.

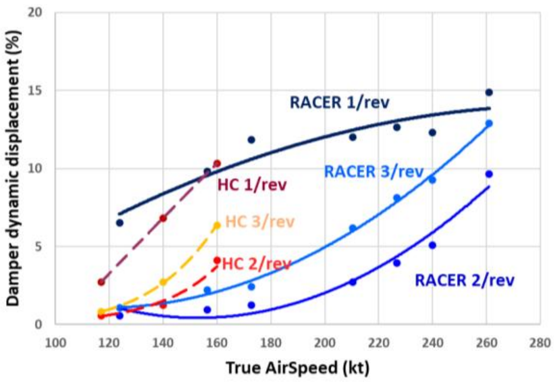

Figure 25: Evolution of measured lead-lag damper displacement amplitude with flight speed.

At high speeds, the aerodynamic load distribution excites the blade's second flapping mode (2.8/rev), generating 2/rev and 3/rev damper motions via flap-lag coupling. Although more pronounced than in a conventional helicopter's flight domain, these loads do not become unmanageable at high speed.

Blade bending moments were analyzed for the most demanding case at 261kt and the results are presented in Figure 26 and Figure 27 for two measurement radial stations at r/R=0.653 and r/R=0.135.

At the outboard station (0.653R), the simulation shows excellent agreement with flight measurements. While higher harmonics are more pronounced in the flight data for the inboard station, overall the comparison is sufficiently predictive to be used in de-risking the blade parts expected life.

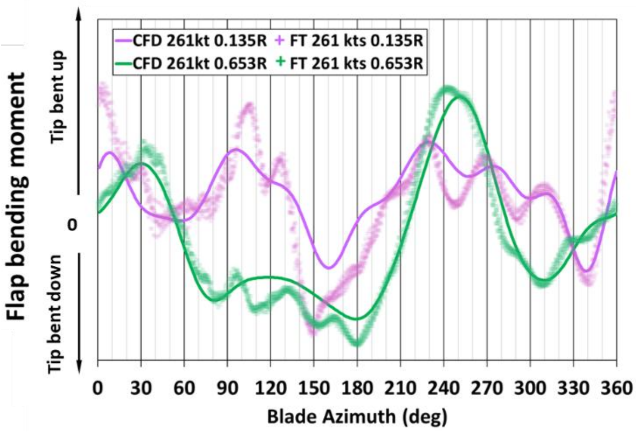

Figure 26: Comparison between CFD and FT data: Flap bending moment as a function of the blade azimuth for 261kt.

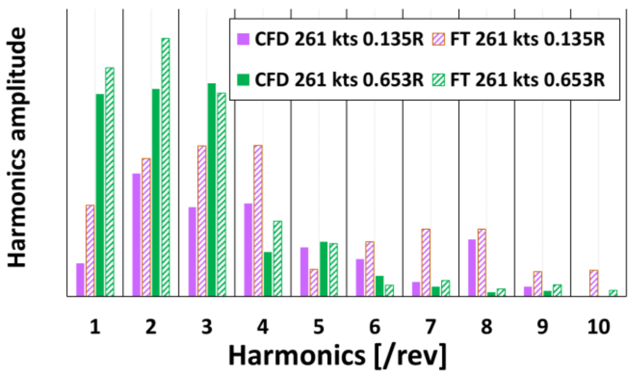

Figure 27: Comparison between CFD and FT data: Flap bending moment harmonic breakdown for 261kts.

At lower speeds, such as 240kt the agreement with flight data is even better, as shown in Figure 28 and Figure 29.

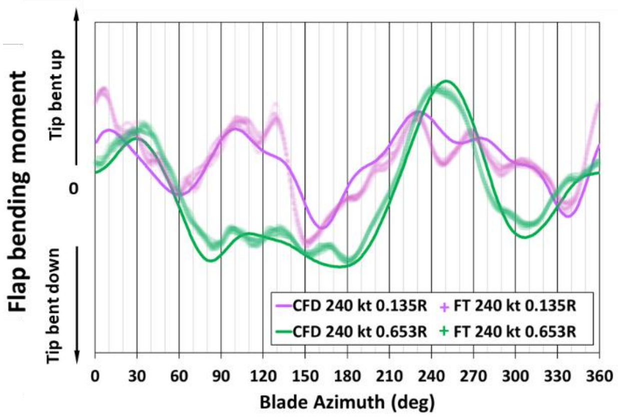

Figure 28: Comparison between CFD and FT data: Flap bending moment as a function of the blade azimuth for 240kt.

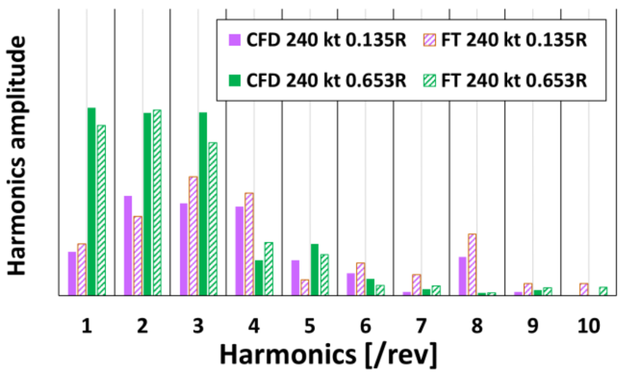

Figure 29: Comparison between CFD and FT data: Flap bending moment harmonic breakdown for 240kts.

5. CONCLUSIONS

This paper demonstrated the successful application of a high-fidelity CFD/CSD simulation toolchain to analyze challenging aeromechanical phenomena on the Airbus RACER demonstrator. The RACER exceeded its target cruise speed (VH) of 220 kts in less than 6 flight hours and this fast achievement is largely based on the predictions of the CFD rotor simulations. After a first validation in the helicopter flight domain (Ref. 3), these simulations were used to predefine the aerodynamic settings of the rotor for the target cruise speed inducing an advance ratio close to 0.6. The flight tests results (Ref. 1) fully validated these settings, thus saving configurations changes and flight hours in an industrial context.

The CFD simulation proved to be predictive not only in terms of peak-to-peak loads, but also regarding time signals, blade stability and harmonic breakdown of loads and motions. Then, as for every rotorcraft, the cruise speed must be secured by the demonstration of the design diving speed (VD, 260+ kts) implying an advance ratio up to 0.7 extending the challenge for the CFD simulation.

The key findings are summarized as follows:

1. The established loose-coupling methodology between the FLOWer (CFD) and CAMRAD II (CSD) codes was successfully applied to the high-speed flight envelope, and the results were validated against available flight test data.

2. Simulations at high advance ratios revealed significant numerical challenges, with trim con-vergence being highly sensitive to the chosen trim strategy. A conventional control-based strategy proved robust and stable, whereas an alternative approach designed for higher physical fidelity (trimming airframe pitch) was prone to undamped oscillations.

3. Detailed analysis identified the primary aerodynamic drivers for high-speed rotor loads: transonic shock formation on the advancing blade, and a combination of reverse flow on the retreating blade. These phenomena intensify as speed increases. The accuracy of the model supports the NR law design to optimize the compromise between the advancing blade and the retreating blade.

4. The numerical instability observed in the high-fidelity trim simulations is attributed to the sensitivity of the blade's elastic torsional response, which causes phase shifts in the computed transonic shock between trim iterations.

5. The stable simulations achieved show good agreement with flight data, providing valuable insights into the rotor's aeroelastic behavior at the edge of the flight envelope.

The strong agreement across multiple components validates the predictive capability of the simulation framework. The results confirm that the toolchain is sufficiently mature to be used in derisking the fatigue life of key rotor components in this extended high-speed flight envelope and establish a solid foundation for its use in analyzing future flight tests.

Future efforts will be directed towards further validating the simulations with new flight test data, investigating numerical damping strategies to stabilize more physically representative trim approaches and extending the analysis to include high load factor maneuvers and the full aircraft configuration.

Authors contact:

Enric Roca León enric.roca@airbus.com

Martin Embacher martin.embacher@airbus.com

Damien Desvigne damien.desvigne@airbus.com

Paul Eglin paul.eglin@airbus.com

6. ACKNOWLEDGMENTS

The RACER project has received funding from the European Union's Horizon 2020 research and innovation program under Clean Sky 2 Grant Agreements CS2-GAM-2014-FRC, CS2-GAM-2014-AIR, and subsequent amendments and versions of those Grants. The authors would like to acknowledge the contribution of CS2 partners and core partners.

7. REFERENCES

1. Eglin, P., Embacher, M, Desvigne, D. and Roca León, E., "Airbus RACER High Speed Demonstrator Flight Tests," Vertical Flight Society 81st Annual Forum Proceedings, Virginia Beach, VA, May 2025.

2. Johnson, W., "Technology drivers in the development of CAMRAD II," AHS Technical Specialists' Meeting on Rotorcraft System Identification, San Francisco, CA, 1994.

3. Roca León, E., Desvigne, D. and Embacher, M., "Understanding flight-test data with CFD rotor simulations: An application case on the H175 helicopter," 48th European Rotorcraft Forum, Winterthur, Switzerland, September, 2022.

4. Potsdam, M., Yeo, H., & Johnson, W., "Rotor Airloads Prediction Using Loose Aerodynamic/Structural Coupling," Journal of Aircraft, Vol. 43, No. 3, May-June 2006, pp. 732-742.

5. Ortun, B., Potsdam, M., Yeo, H., Van Truong, K., "Rotor Loads Prediction on the ONERA 7A Rotor Using Loose Fluid/Structure Coupling," Journal of the American Helicopter Society, Vol. 62, No. 3, July 2017.

6. Menter, F.R., "Two-equation eddy viscosity turbulence model for engineering applications," AIAA J. Vol 32, 8, pp. 1598-1605, 1994.

7. Yeo, H., Potsdam, M., and Ormiston, R. A., "Rotor Aeroelastic Stability Analysis Using Coupled Computational Fluid Dynamics/Computational Structural Dynamics," Journal of the American Helicopter Society, Vol. 56, (4), Oct. 2011.

8. Embacher, M., Keßler, M., Dietz, M., & Krämer, E., "Coupled CFD-Simulation of a Helicopter in Free-Flight Trim," Am. Helicopter Soc., 66th Annual Forum Proceedings, Phoenix, Arizona, USA, 2010.

9. Moretti, R., Richez, F., Ortun, B. & Yeo, H. "Rotor loads prediction on UH-60A flight test using loose fluid/Structure coupling," Vertical Flight Society, 79th Annual Forum Proceedings, West Palm Beach, Florida, USA, May 2023.

10. Kufeld, R.M., et al., "UH-60A Airloads Flight Test Program: Data Counter 8513," NASA/TM2019220317, December 2019.

11. Casolaro, D., "STORM, the New Airbus Rotorcraft Simulation Tool Based on 60 Years of Cumulated Experience in Digital Flight Physics," 48th European Rotorcraft Forum, Winterthur, Switzerland, Sept. 2022.

12. Desvigne, D., & Embacher, M., "Analyzing Low-Speed Rotor-Fuselage Interactions: A Comparative Study of Simulations and Flight-Test Data on H175," 50th European Rotorcraft Forum, Marseille, France, Sept. 2024.

13. Kroll, N., Eisfeld, B., & Bleeke, H., "The navier-stokes code FLOWer," Notes Numer. Fluid Mech. 71, 58-71 (1999).

14. Öhrle, C., Frey, F., Thiemeier, J., Kessler, M., Krämer, E., Embacher, M., Cranga, P., Eglin, P., "Compound Helicopter X3 in High-Speed Flight: Correlation of Simulation and Flight Test", Vertical Flight Society 75th Annual Forum, Philadelphia, Pennsylvania, USA, May 13-16, 2019.

15. Potsdam, M., Datta, A., Jayaraman, B., "Computational Investigation And Fundamental Understanding Of A Slowed UH-60A Rotor At High Advance Ratios", AHS 68th Annual Forum, Fort Worth, TX, May 1-3, 2012.

16. Frey, F., Thiemeier, J., Öhrle, C., Kessler, M., Krämer, E., “Aerodynamic Interactions on Airbus Helicopters’ Compound Helicopter RACER in Cruise Flight”, Vertical Flight Society 75th Annual Forum & Technology Display, Philadelphia, USA, May 13–16, 2019.
17. Lentine, F.P. et.al., “Research in Maneuverability of the XH-51A Compound Helicopter”, USAAVLABS Technical Report 68-23, June 1968.
18. Ormiston, R.A., “Revitalising advanced rotorcraft research – and the compound helicopter”, The Aeronautical Journal, January 2016, Volume 120 No 1223, pp. 83 – 129.